## †Electronic Supplementary Information

# Floatable Photocatalyst to Synergistically Promote CO2 Reduction and Water Oxidation by Creating Oriented Charge Separation across Tri-phase Interface

Yangen Xie[a][b], Min Wang[c], Qiang Huang[a][b], Qing Huang[a][b], Bo Sheng[a][b], Wenjing Song[a][b], Hua Sheng*[a][b] and Jincai Zhao[a][b]

[a] Key Laboratory of Photochemistry, Beijing National Laboratory for Molecular Sciences, Institute of Chemistry Chinese Academy of Sciences, Beijing 100190, PR China
[b] University of Chinese Academy of Sciences, Beijing 100049, PR China
[c] Shanghai Key Laboratory of Green Chemistry and Chemical Processes, School of Chemistry and Molecular Engineering, East China Normal University, Shanghai 200062, China

*Corresponding Author Email: hsheng@iccas.ac.cn

## Methods

### Chemicals

$CuCl_2$ and polyvinylpyrrolidone (PVP, m.w.10000) were procured from Macklin Biochemical Technology Corporation (Shanghai, China). NaOH, ascorbic acid (AA), C2H5OH and acetone were sourced from Sinopharm Chemical Reagent Corporation (Shanghai, China). The Ag target material was obtained from Jiuyuexincai corporation (Hebei, China). Diisopropylamino titanium was purchased from Aimouyuan Scientific Equipment Corporation (Nanjing, China). Na2S, rhodamine B (RhB), N,N-diethyl-p-phenylenediaminehorseradish (DPD), peroxidase (POD), $KH_2PO_4$, $K_3PO_4$ and Methyl viologen dihydrate ($MV^{2+}\cdot 2H_2O$) were purchased from Aladdin Chemical Reagent Corporation (Shanghai, China). PTFE and cellulose filter membrane were purchased from J&K Scientific Corporation (Beijing, China). Deionized water (DI water, 18.25 $M\Omega\cdot cm^{-1}$) supplied by an Ultra Pure Water Purification System was used throughout the whole experimental process.

### Synthesis of $Cu_2O$ nanoparticle

$Cu_2O$ nanoparticles were synthesized following a previously reported protocol.[1] Initially, 134.5 mg $CuCl_2$ and 5g PVP were dissolved in 100 mL water to form a pale blue solution, which was then stirred and heated at 55 °C for 30 min. Subsequently, 10 mL of a 2 M NaOH solution was added dropwisely to the above $CuCl_2$/PVP solution and stirred. The solution gradually turned turbid, changing its color from pale blue to dark blue and finally to dark brown. After 30 min, 10 mL of an AA solution (0.6 M) was added into the mixture while maintaining the temperature at 55 °C, leading to the suspension's gradual transformation into a dark red color. Following a 3 h reaction, the suspension was cooled to room temperature and purified by centrifugation at 11000 rpm, and then redispersed in DI water for 5 cycles to obtain clean $Cu_2O$ nanoparticles. The nanoparticles were collected and dried in the vacuum drying oven at 60 ℃ overnight.

### Preparation of $Cu_2O$/Ag/$TiO_2$ hybrid photocatalyst with oriented alignment (OA-photocatalyst)

The OA-photocatalyst was fabricated via a layer-by-layer approach. Initially, 2 mg of as-synthesized $Cu_2O$ was dispersed in 50 mL $C_2H_5OH$ and anchored onto PTFE membrane through vacuum filtration, forming a $Cu_2O$ layer that was subsequently dried under vacuum at 60 °C overnight. The Ag layer was then stacked onto the $Cu_2O$ layer using by e-beam evaporation from an Ag target. This evaporation procedure used 2.3% power magnitude of power at a rate of 0.03 A/s. After 1000 s evaporation, a 30 nm Ag layer was deposited on top of the $Cu_2O$ layer ($Cu_2O$/Ag). The following deposition of the $TiO_2$ layer was achieved through atomic layer deposition (ALD). During ALD deposition, the as-prepared $Cu_2O$/Ag membrane was placed in the ALD chamber at a temperature of 200 °C, with the gas flow rate introducing precursors or water vapor set at 80 sccm. In each ALD cycle, the diisopropylamino titanium precursors (preheated at 120 °C) were first introduced in a 0.02 s pulse, followed by 30 s Ar purging. This resulted in a monolayer adsorption of diisopropylamino titanium on the Ag layer surface. The subsequent pulse of water vapor lasted 2 s, which reacted with diisopropylamino titanium to produce $TiO_2$ monolayer, then the byproducts

and residue reagents were removed by Ar flow for another 30 s. One ALD cycle resulted in the growth of an amorphous $TiO_2$ layer of 0.35 Å thickness, by repeating the cycle 1430 times, a 50 nm $TiO_2$ layer was obtained.

**Preparation of hybrid photocatalyst with random alignment (RA-photocatalyst)**

To fabricate the RA-photocatalyst, we followed the same procedure as for the OA-photocatalyst, with the exception of using a cellulose membrane as support instead of the PFTE membrane. After dissolving the cellulose support in acetone, the nanoparticles of $Cu_2O/Ag/TiO_2$ were obtained, which were further anchored onto a PTFE membrane through vacuum filtration.

**Characterization**

The morphologies of the photocatalysts and corresponding EDS analysis were observed using field scanning electron microscopy (FESEM, Hitachi SU8020, Japan). And transmission electron microscopy (TEM, Hitachi HT7700, Japan) was also utilized to describe the morphology of photocatalyst. Crystal structures were determined by X-ray diffraction (XRD, Rigaku D/max 2500, Japan). Contact angles were measured using an OCA 20 contact angle system (Dataphysics, Germany), and the reported values are averages derived from more than three positions. UV-Vis absorption spectra of RhB and the quantification of the $H_2O_2$ were obtained using a UV-Visible spectrophotometer (Cary 3500, Agilent, America). X-ray photoelectron spectroscopy (XPS) spectra were collected on an ESCALab250Xi instrument (Thermo Fisher, America), with binding energies calibrated by the C 1s electron peak (BE = 284.8 eV). Transient surface photovoltage measurements were conducted using the CEL-TPV2000 instrument (CeauLight, China). In situ irradiated X-ray photoelectron spectroscopy was determined. Meanwhile, a 300W Xenon light (Zhongjiaojinyuan Co. Ltd., China) was placed ca. 30 cm away from the prepared samples during the semi-in-situ-XPS characterization to investigate the electron density changes on prepared samples under light irradiation. Raman spectra (LabRAM Odyssey Nano) experiments were performed with a microscope equipped with a 365 nm laser and a homemade cell. The 50% Neutral Density (ND) filter, 600 grating, and 50X visible long-work-distance lens were used during the operation. A Leica 50× water immersion objective was used for illumination and collection in these measurements. For all the Raman tests in this work, the Rayleigh and monocrystalline Si signals were calibrated to 0 and 520.75 $cm^{-1}$, respectively. The LED could be turned on or off to assess photoinduced processes that were analyzed from the data acquired from the surface in the Raman shift range between 200 and 2200 $cm^{-1}$. The exposure time was set to 10 min with 3-times accumulations.

**Confocal laser scanning microscopy measurement**

Confocal laser scanning microscopy (CLSM) measurements were conducted using an Olympus FluoView FV1000 laser confocal microscope. Typically, a 100 μL of RhB-labeled aqueous solution (0.01 mg/mL) was deposited onto a confocal dish. Subsequently, the bare PTFE membrane or the membrane with

OA-photocatalyst (the $TiO_2$ side facing down) was placed on the aqueous surface (as illustrated in Figure S7a). A 405 nm laser served as the excitation light source, and the confocal microscope was equipped with a 20× objective lens.

**Photocatalytic activity test**

The photocatalytic activity test was conducted in a homemade photocatalytical reactor consisting of a stainless-steel chamber with embedded quartz windows on two sides. The setup also included a cooling system, a gas sampling port and a pressure gauge. The gas circulation system was filled with $CO_2$ in a total gas volume of 150 mL, while the water volume remained at 17 mL. Two 300 W Xenon lamps equipped with an IR cutter (≥ 800 nm) were used as the light source to irradiate the photocatalyst membrane from both the top and bottom, maintaining a constant light intensity of 300 $mW \cdot cm^{-2}$. Before irradiation, a quartz cell containing 17 mL water was positioned inside the chamber, and the photocatalyst membrane was floated on the water surface. The chamber was then purged with pure $CO_2$ (≥ 99.99%, the flow rate is 150 $mL \cdot min^{-1}$) for 30 min. During the photocatalytic reaction, the temperature of the chamber was maintained at 25 °C using a low-temperature water circulation system. To assess the performance of the photocatalyst under gas-solid conditions, the photocatalyst membrane was placed in the empty quartz cell, and 1 mL water was injected into the chamber after filled with $CO_2$. For the water-solid phase, the photocatalyst membrane was submerged beneath the water surface. After a 3h reaction period, the gaseous products (CO, $CH_4$ and $O_2$) were analyzed using a FuLi GC 9790Plus gas chromatograph (Carrier gas: Argon, Column: molecular sieve 5, Detector: FID and TCD). The $H_2O_2$ generated in the aqueous phase was quantified by the DPD-POD method as reported. [2]

The isotope experiment was tested using the same reactor described above. The OA-photocatalyst was floated on the $H_2{}^{18}O$ in the quartz cell. The reactor was evacuated and filled with $^{13}CO_2$ gas. After 3 h irradiation, the gas products were detected by a gas chromatography-mass spectrometer (GC-MS, Agilent Technologies, America).

The apparent quantum yield (AQY) was measured by inserting band-pass filters with different wavelengths between the light source and the reactor. AQY of carbon products over the OA-photocatalyst at tri-phase was calculated as follows:

$AQY=\frac{2\times nCO+8\times nCH4}{nphotons}\times 100\%$, $n_{photons}=\frac{I\lambda}{hc}$; where $n_{CO}$, $n_{CH4}$ and $n_{photons}$ represent the numbers of CO, $CH_4$ and incident photons, respectively. I, λ, h and c represent the radiant energy density, the wavelength of light, Planck's constant, and the speed of light, respectively.

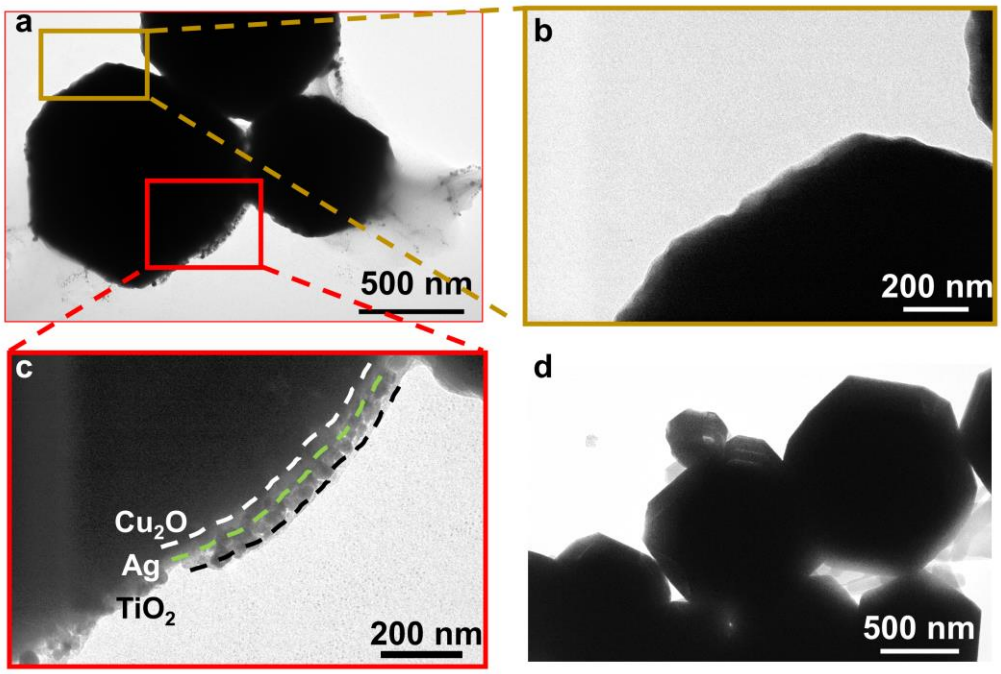


**Figure S1.** Transmission Electron Microscopy (TEM) images of (a) hybrid $Cu_2O$-Ag-$TiO_2$ nanoparticles obtained from Step iv in Figure 1, (b) and (c) correspond to magnified sections of (b) (indicated by red and gold frame, respectively), highlighting the deposited Ag and $TiO_2$ layers onto one side of the as-synthesized $Cu_2O$ nanoparticles and (d) as-synthesized $Cu_2O$ nanoparticles.

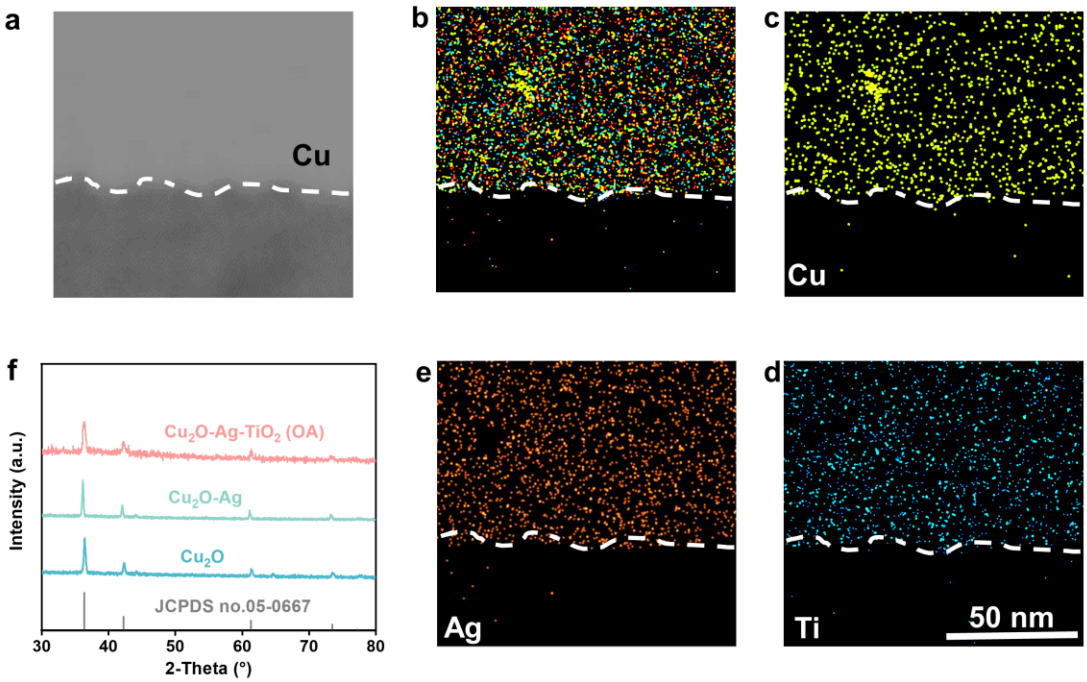


**Figure S2.** (a) Field Emission Scanning Electronic Microscopy (FE-SEM) images of RA-photocatalyst; (b-e) EDS mapping of RA-photocatalyst (The region indicated by red frame in (a)); (f) X-ray Diffraction (XRD) patterns of as-synthesized $Cu_2O$, $Cu_2O$-Ag, $Cu_2O$-Ag-$TiO_2$.

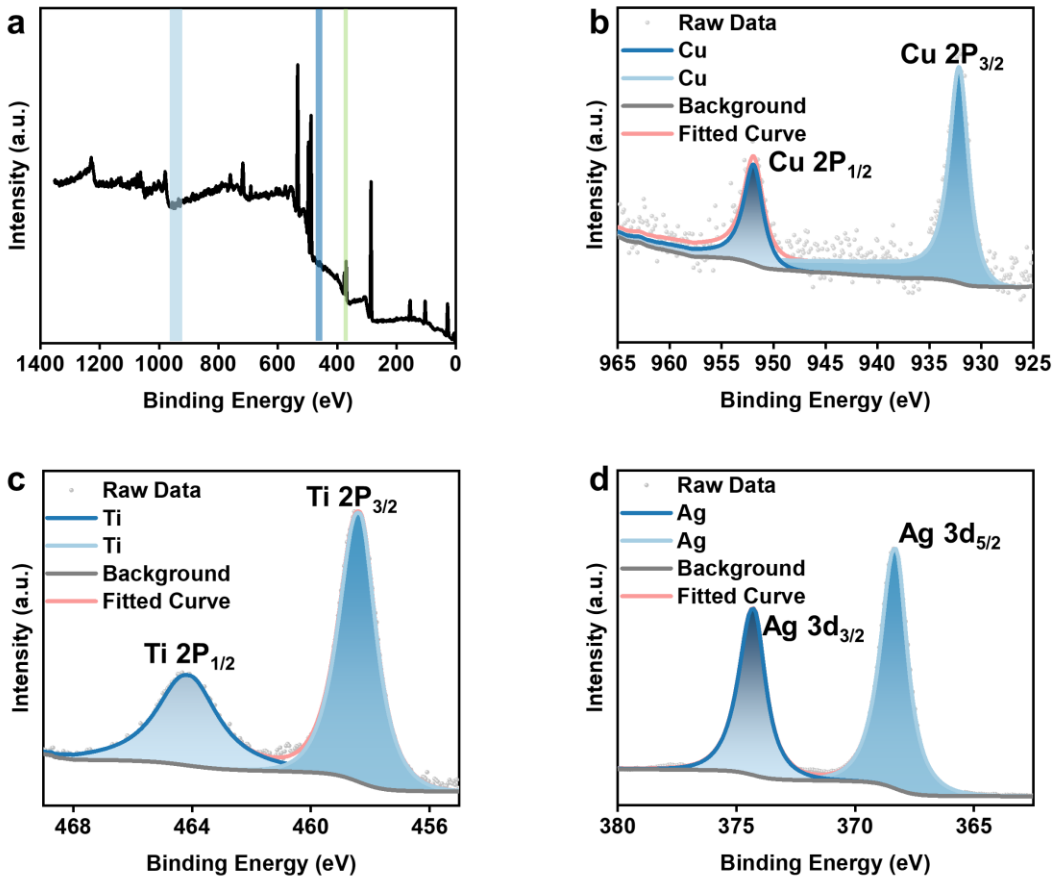


**Figure S3.** XPS spectra of $Cu_2O$-Ag-$TiO_2$ nanoparticle: (b) Cu 2*p*, (c) Ti 2*p* and (d) Ag 3*d* XPS spectra.

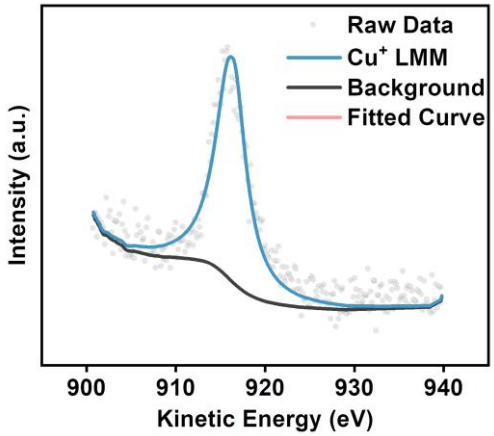


**Figure S4.** Auger spectra of $Cu_2O$-Ag-$TiO_2$ nanoparticle.

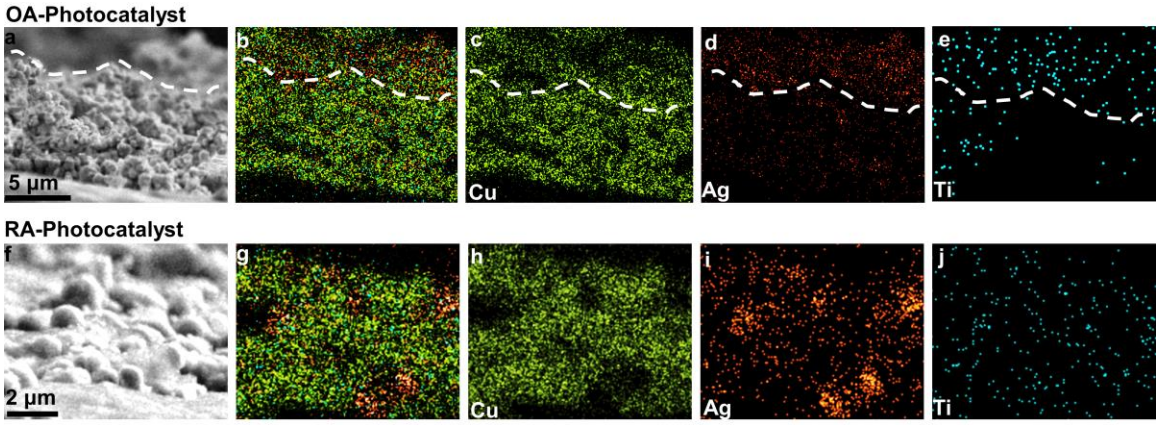


**Figure S5.** (a) Field Emission Scanning Electronic Microscopy (FE-SEM) images at microscale of OA-photocatalyst; (b-e) EDS mapping of OA-photocatalyst (The region indicated by frame in (a)); (f) Field Emission Scanning Electronic Microscopy (FE-SEM) images at microscale of RA-photocatalyst; (g-j) EDS mapping of OA-photocatalyst (The region indicated by frame in (f)).

The distribution of Ag and Ti on RA-photocatalysts appears uniform across the entire image, whereas on OA-photocatalysts, Ag and Ti are predominantly concentrated in the top portion of the image, with the top part of the Cu mapping being lighter than other regions.

The less defined boundaries at larger scales result from the initial embedding of $Cu_2O$ nanoparticles into the membrane via filtration, leading to various ratios of $Cu_2O$ embedding within membrane pores and a rough surface of exposed $Cu_2O$ layer in the micrometer scale. Consequently, after loading Ag and $TiO_2$, the top of Cu mapping of one $Cu_2O$-Ag-$TiO_2$ structure may overlap with the Ag, Ti mapping of another $Cu_2O$-Ag-$TiO_2$ structure. Furthermore, the $Cu_2O$-Ag-$TiO_2$ structure resembles more of a core-shell structure than a flat-layer stacking structure, contributing to partial overlapping in cross-section element mapping.

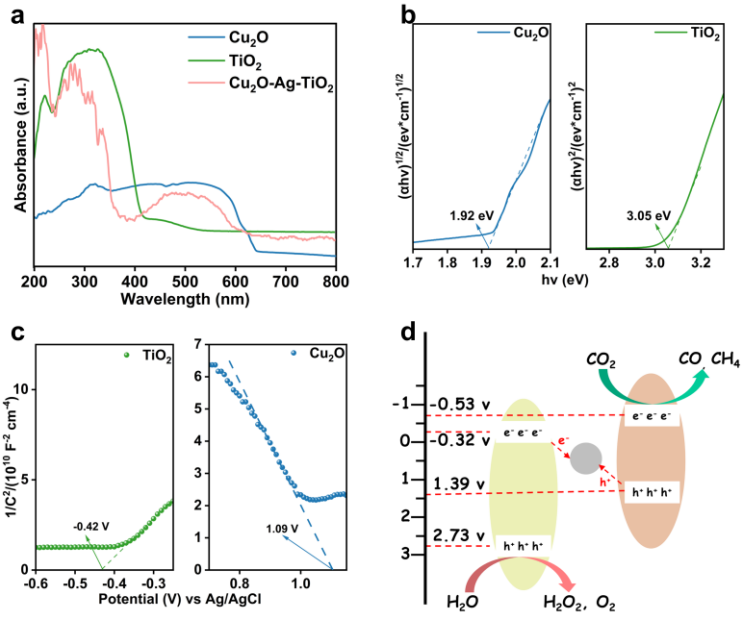


**Figure S6. (a)** UV-Vis spectra of $Cu_2O$, $TiO_2$ and $Cu_2O$-Ag-$TiO_2$; (b) Tauc plots of $Cu_2O$, $TiO_2$; (c) Mott–Schottky plots of $Cu_2O$, $TiO_2$; (d) Schematic illustration of the band structure of $Cu_2O$-Ag-$TiO_2$.

As shown in UV-Vis spectra (Figure S6a), the pristine $Cu_2O$ nanoparticle exhibits an absorption edge at 645 nm, with a 1.92 eV band gap calculated by Tauc plot (Figure S6b), while pure ALD-deposited $TiO_2$ displays a 3.05 eV band gap. The hybrid structure of $Cu_2O$-Ag-$TiO_2$ exhibits close absorption edge with $Cu_2O$, but its UV adsorption is enhanced owing to the presence of $TiO_2$ component. In Mott-Schottky plots (Figure S6c), the positive slope of $TiO_2$ indicates its nature of n-type semiconductor. The Fermi level of ALD-$TiO_2$ is calculated to be -0.22 eV, since the conduction band (CB) in n-type semiconductor is generally regarded as 0.1 eV more negative than Fermi level, the CB level of ALD-$TiO_2$ can be estimated as -0.32 eV. With a band gap of 3.05 eV, its valance band (VB) potential can be determined as 2.73 eV. In comparison, $Cu_2O$ is determined to be p-type semiconductor based on the negative slope in Motty-Schottky plots. The combination of p-type $Cu_2O$ and n-type $TiO_2$ would favor the formation of Z-scheme hybrid photocatalyst. The band levels of $Cu_2O$ can be determined by the similar calculation, with CB and VB level at -0.53 and 1.39 eV. In the original manuscript, the combined XPS, TPV and redox indicator experiments had that confirm the formation of Z-scheme photocatalyst on $Cu_2O$-Ag-$TiO_2$, therefore, the band structure of $Cu_2O$-Ag-$TiO_2$ can be determined as illustrated ((Figure S6d).

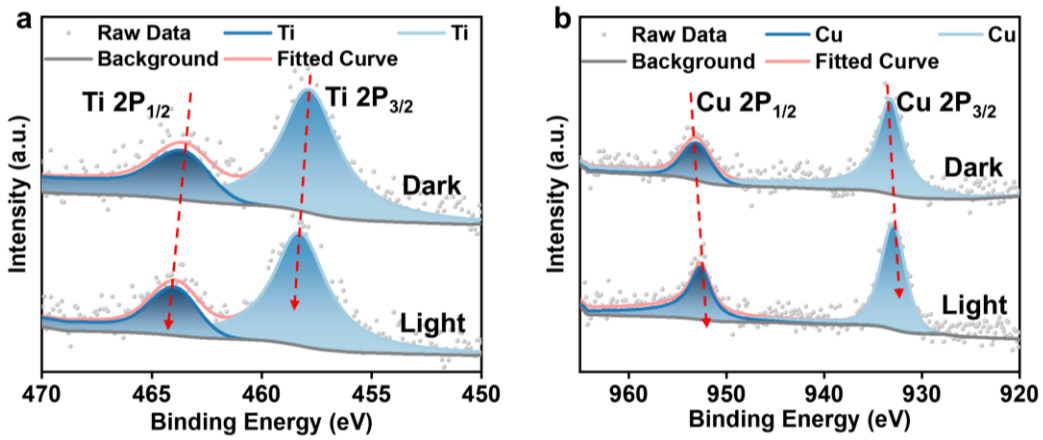


**Figure S7.** Semi-in-situ XPS spectra of $Cu_2O$-Ag-$TiO_2$ nanoparticle: (a) Cu 2*p*, (b) Ti 2*p* before and after light irradiation.

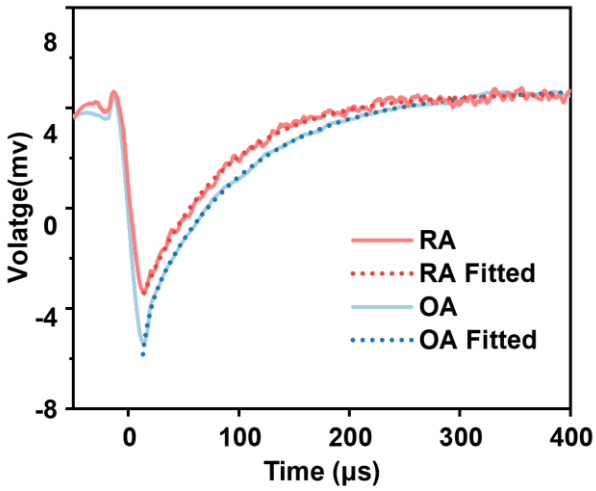


**Figure S8.** Transient photovoltage spectra (TPV) of OA-photocatalyst (blue) and RA-photocatalyst (red).

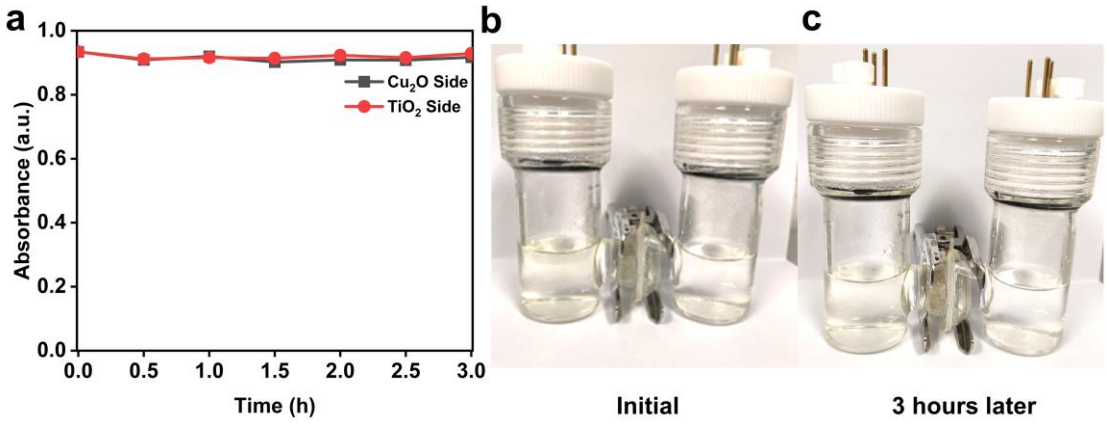


**Figure S9.** (a): The unchanged UV-Vis absorbance at maximum absorbance of $MV^{2+}$ (258 nm) when simply loading $MV^{2+}$ on $Cu_2O$ (black line) and $TiO_2$ side (red line) of the H-cell, respectively; (b,c): digital images of redox indicator ($MV^{2+}$ and $I^-$) experiment in 3 hours without illumination.

During 3 h dark-contact, the absorbance of $MV^{2+}$ exhibited no notable change indicating the limited adsorption of $MV^{2+}$ on both sides of the OA-photocatalyst, in the meanwhile, no color change in the $MV^{2+}$ solution was monitored, suggesting the absence of $MV^{+}$ formation. This result indicates that a dark contact of MV2+ to the OA-photocatalyst does not induce its transformation to $MV^{+}$ or a color change. The only mechanism for transforming colorless $MV^{2+}$ to blue $MV^{+}$ is through reduction reactions.

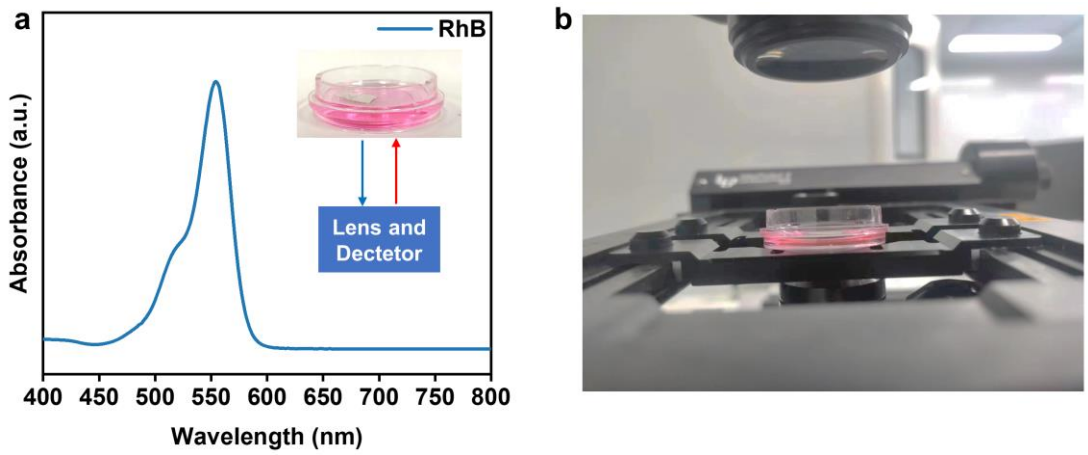


**Figure S10.** (a) UV-vis spectrum of RhB; (b) photo for the operation of confocal laser scanning microscopy (CLSM).

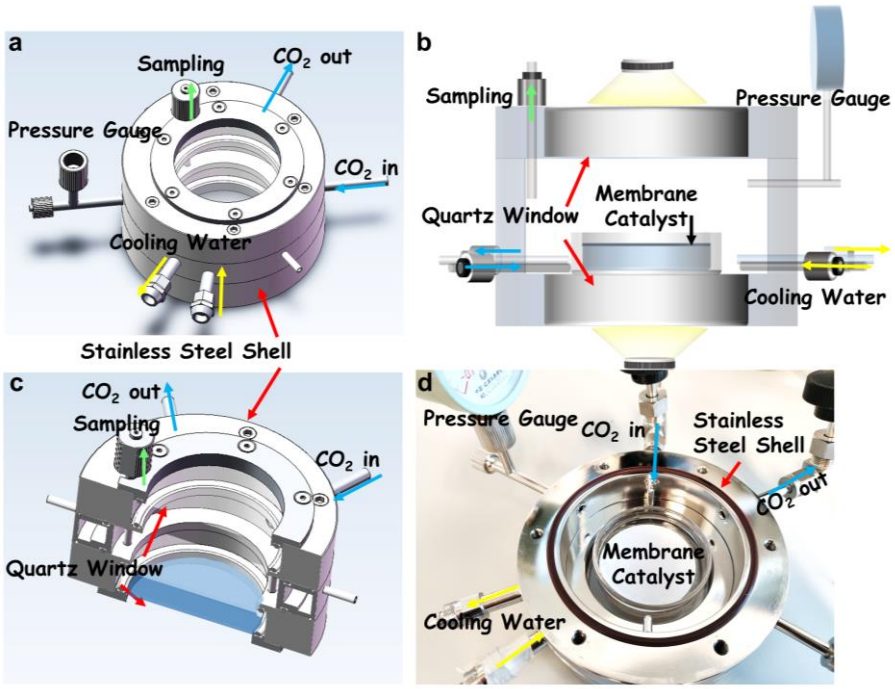


**Figure S11.** Schematic illustration and photo of the home-made reactor for the activity test.

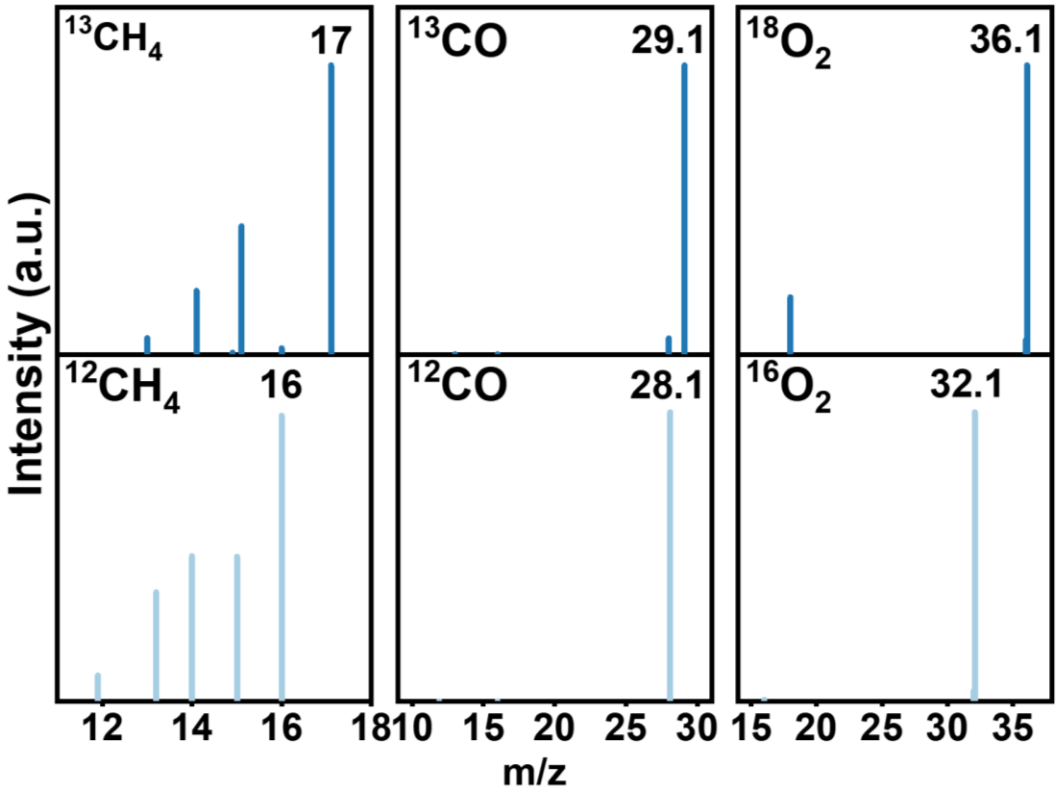


**Figure S12.** $^{12}CO_2$, $H_2{}^{16}O$ and isotope-labeled $^{13}CO_2$, $H_2{}^{18}O$ photocatalytic tests screened by GC-MS

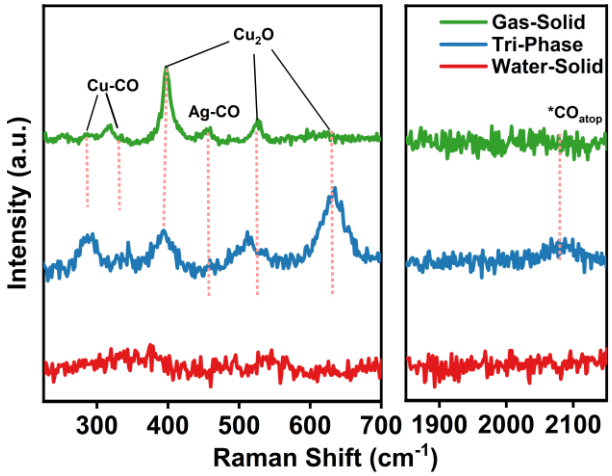


**Figure S13.** Raman spectra of $Cu_2O$-Ag-$TiO_2$ reacted with $CO_2$ of 10 min 365 nm irradiation under various circumstances.

In gas-solid and tri-phase reactions under illumination, several $CO_2$RR-related intermediates emerge, such as Cu-CO (280 and 350 $cm^{-1}$) and Ag-CO (470 $cm^{-1}$). Notably, a distinct top-bounded *CO band (2080 $cm^{-1}$) is more pronounced in tri-phase conditions, indicating enhanced $CO_2$RR reduction efficiency compared to gas-solid conditions.[3-5] Conversely, water-solid reactions show no $CO_2$RR-related bands or top-bounded *CO, suggesting an inability for $CO_2$RR to compete with HER, and thus, no observable $CO_2$RR reduction in Raman spectra. These Raman results align with activity tests, underscoring the pivotal role of reaction environment in influencing the competition between $CO_2$RR and HER.

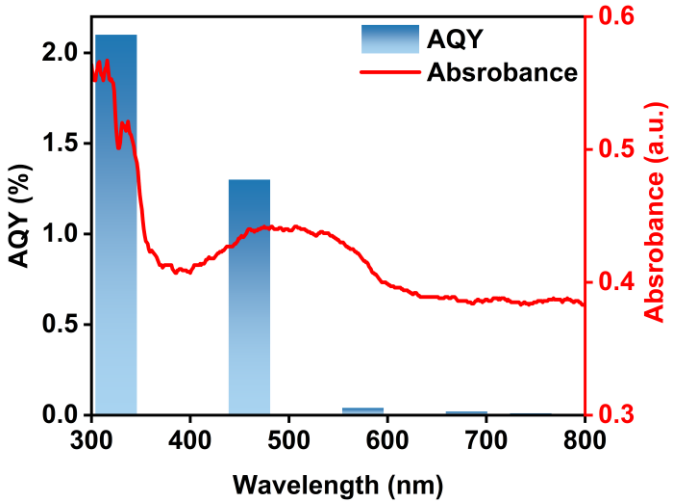


**Figure S14.** Apparent quantum yields spectra of $Cu_2O$-Ag-$TiO_2$ under various monochromatic wavelength illumination (325, 460, 575, 680, 740 nm) under tri-phase condition.

The highest AQY 2.1% at 325 nm. The superior performance comes from our Z-scheme structure high efficient utilization of light at tri-phase.

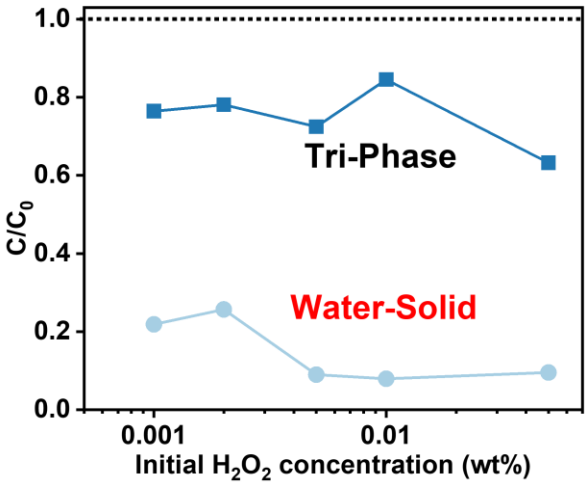


**Figure S15.** $H_2O_2$ degradation curve under various initial $H_2O_2$ concentration

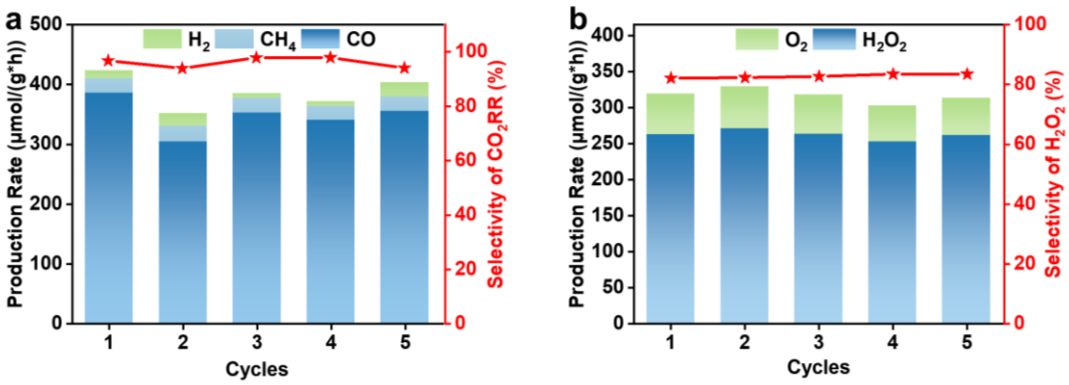


**Figure S16.** Cyclic activity test of photocatalytic (a) $CO_2RR$ and (b) WOR on OA-photocatalyst under tri-phase circumstances.

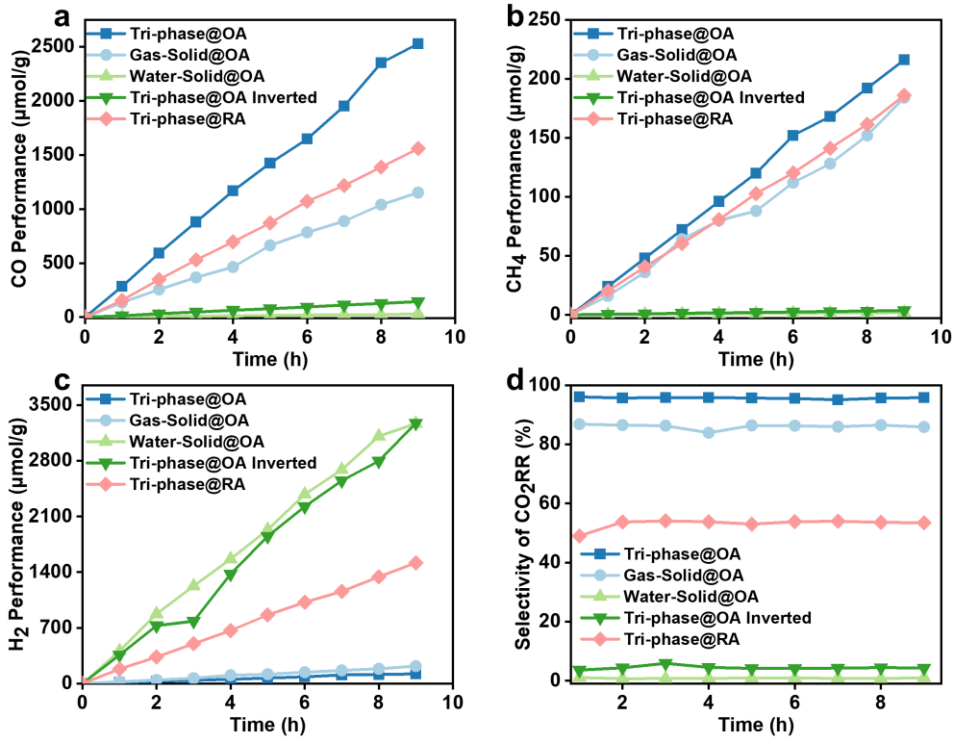


**Figure S17.** (a-c) Generation kinetics of products in reductive half-reaction ((a) CO, (b) $CH_4$ and (c) $H_2$) for tri-phase OA-photocatalyst, gas-solid OA-photocatalyst, water-solid OA-photocatalyst, inverted OA-photocatalyst under tri-phase condition and tri-phase RA-photocatalyst. (d) Time-dependent selectivity of $CO_2RR$ products by molar ratio.

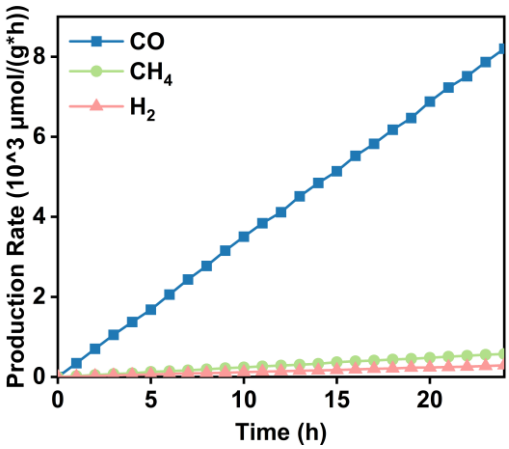


**Figure S18.**Time dependent $CO_2$RR performance of $Cu_2O$-Ag-$TiO_2$ under tri-phase condition in 24 hours.

The CO $CH_4$ and $H_2$ generation are linearly with time, no notably decay in the performance was observed under continuous 24 illumination, consolidating the robustness of our photocatalyst.

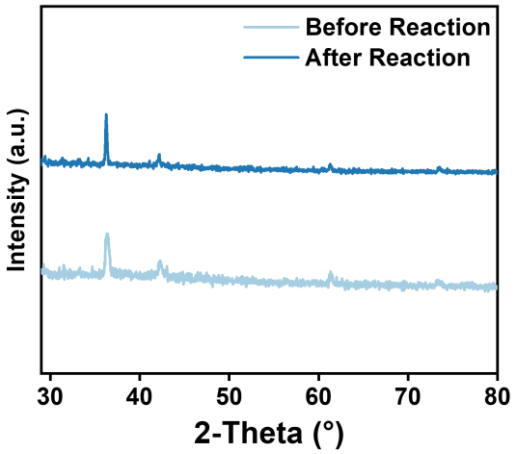


**Figure S19.** XRD of OA-photocatalyst before and after 3 hours' reaction.

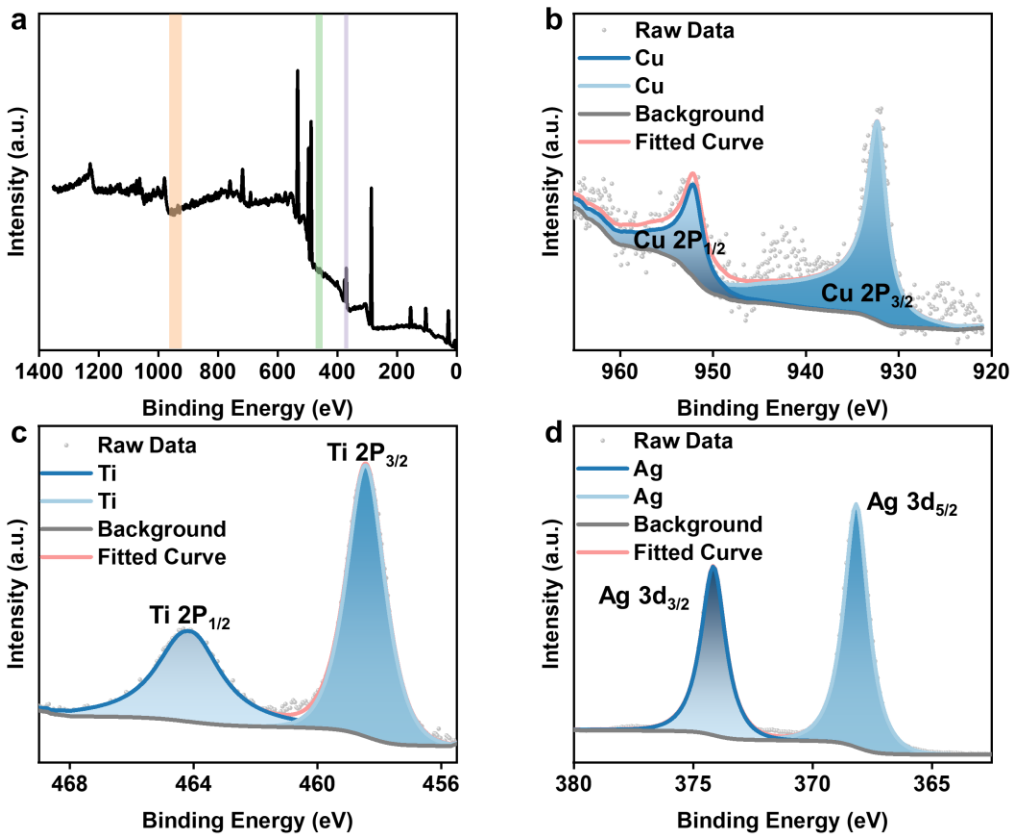


**Figure S20.** XPS of OA-photocatalyst after 3 hours' reaction (b) Cu 2*p* XPS analysis; (c) Ti 2*p* XPS analysis; (d) Ag 3*d* XPS analysis.

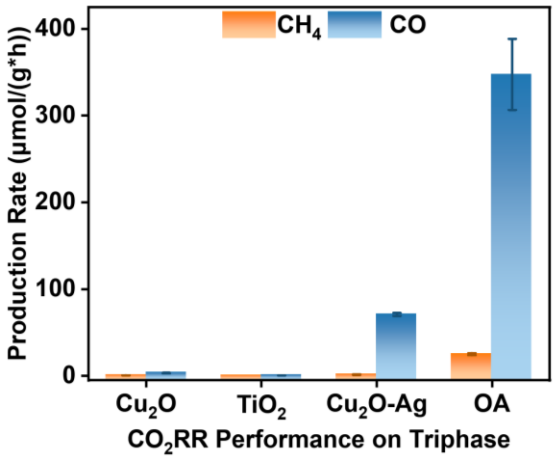


**Figure S21.** Photocatalytic $CO_2$ reduction of individual $Cu_2O$ nanoparticle, ALD-deposited $TiO_2$ layer and the hybrid $Cu_2O$-Ag, which are all deposited on PTFE membrane.

The performance of each ingredient of OA-photocatalyst obvious decreased when comparing to the pristine OA-photocatalyst indicates that the performance of $CO_2RR$ mainly comes from the OA-photocatalyst rather than the interference of ingredients of OA-photocatalyst.

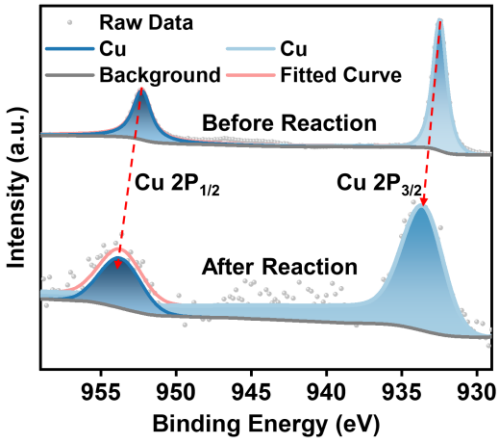


**Figure S22.** XPS spectra of $Cu_2O$ nanoparticle before and after light 3 hours' irradiation.

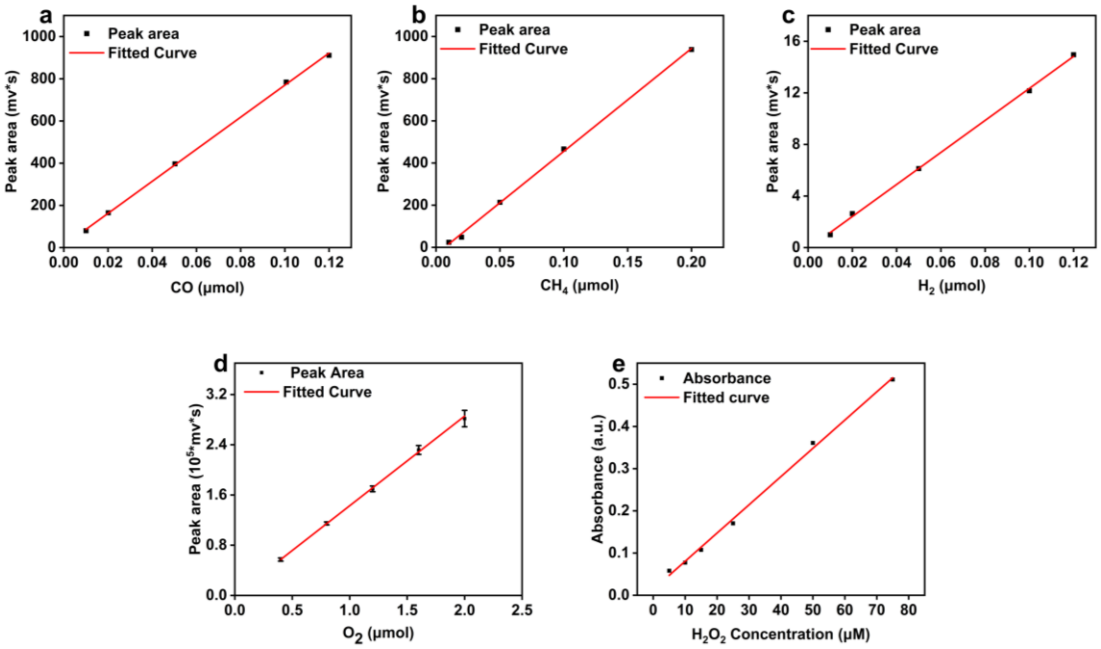


**Figure S23.** Standard curve for the quantification of (a) CO, (b) $CH_4$, (c) $H_2$, (d) $O_2$ and (e) $H_2O_2$.

**Table S1.** Fitting parameters of Transient Photovoltage Spectra (TPV) curve

| Species | $y_0$ | $A_1$ | $\tau_1$ | $A_1$ | $\tau_1$ | $A_1$ | $\tau_1$ | $R^2$ |
|---|---|---|---|---|---|---|---|---|
| **OA** | 4.7558 | -0.7524 | 32.370 | -9.9257 | 95.001 | -16.394 | 5.3693 | 0.99887 |
| **RA** | 5.7256 | -3.2519 | 74.615 | -3.5492 | 74.621 | -3.6235 | 74.620 | 0.99523 |

**Table S2.** Fitting parameters of the standard curves

| Species | Slope | Intercept | $R^2$ |
|---|---|---|---|
| **CO** | 7597.1 | 10.077 | 0.99949 |
| **$CH_4$** | 4880.7 | -32.786 | 0.99913 |
| **$H_2$** | 124.16 | -0.07157 | 0.99909 |
| **$H_2O_2$** | 0.00669 | 0.01362 | 0.99717 |
| **$O_2$** | 1.4266 | 0.00261 | 0.99957 |

**Table S3.** Apparent quantum yields of $Cu_2O$-Ag-$TiO_2$ under various wavelength illumination at tri-phase condition

| Wavelength (nm) | AQY (%) |
|---|---|
| 325 | 2.1 |
| 460 | 1.3 |
| 575 | 0.04 |
| 680 | 0.02 |
| 740 | 0.01 |

**Table S4.** Comparison of photocatalysts for $CO_2$ photocatalysis under various conditions with this work

| Photocatalyst | $CO_2$RR yield (μmol/(g*h)) | $H_2O_2$ yield (μmol/(g*h)) | Light (nm) | Condition | Ref. |
|---|---|---|---|---|---|
| **$TiO_2$-Ag-$Cu_2O$** | **347.4 (CO), 25.1 ($CH_4$)** | **259.1** | **λ:320-780** | **$CO_2$, $H_2O$, Tri-phase** | **This work** |
| $Cu_2O/TiO_2$ | 2.11 (CO) | N.A. | λ ≥ 305 | $CO_2$,$H_2O$, Water-Solid | 6 |
| Pt-$Cu_2O$ $TiO_2$ | 0..05 (CO), 1.42 ($CH_4$) | N.A. | λ:300-400 | $CO_2$, $H_2O$, Water-Solid | 7 |
| Cu−SA/D−ZIS | 112.5 (CO) | N.A. | λ ≥ 420 | $CO_2$, $H_2O$, Gas-Solid | 8 |
| $CsPbBr_3$-FCA | 132.8 (CO), 1.6 ($C_2H_4$) | N.A. | AM 1.5G | $CO_2$, $H_2O$, Gas-Solid | 9 |
| Ultrathin bismuthene | 14.32 (CO), 4.69 ($CH_4$) | N.A. | Full Range | $CO_2$, $H_2O$, Gas-Solid | 10 |
| Fe SACs-$TiO_2/SrTiO_3$ | 93 (CO), 53 ($CH_4$) | N.A. | AM 1.5G | $CO_2$, $H_2O$, Gas-Solid | 11 |
| VS-$SnS_2$ | 25.71 (CO) | N.A. | Full Range | $CO_2$, $H_2O$, Gas-Solid | 12 |
| SACs $Cu_1/N_2$CV-CN | 11.12 (CO) | 2.248 | AM 1.5G | $CO_2$, $H_2O$, Gas-Solid | 13 |
| $Cu_4(SO_4)(OH)_6$ nanosheet | 21.95 (CO), 4.11 ($CH_4$) | N.A. | AM 1.5 G | $CO_2$, $H_2O$, Tri-phase | 14 |
| TCOF-$MnMo_6$ | 37.25 (CO) | N.A. | 400-800 | $CO_2$, $H_2O$, Gas-Solid | 15 |
| Ni-MOF (PCN-601) | 10.1 ($CH_4$) | N.A. | λ ≥ 410 | $CO_2$, $H_2O$, Gas-Solid | 16 |
| $Bi_4Ti_3O_{12}$ | 15.1 (CO) | N.A. | Full Range | $CO_2$, $H_2O$, Gas-Solid | 17 |
| CoDACs | 12.7 (CO), 19.5 ($CH_4$) | N.A. | AM 1.5G | $CO_2$, $H_2O$, Gas-Solid | 18 |
| AuSA/$Cd_{1-x}S$ | 32.2 (CO), 11.3 ($CH_4$) | N.A. | Full Range | $CO_2$, $H_2O$, Gas-Solid | 19 |
| Mn, C-ZnO CTSHSs | 0.83 (CO) | N.A. | Full Range | $CO_2$, $H_2O$, Gas-Solid | 20 |
| $TiO_2/CsPbBr_3$ | 9.02 (CO) | N.A. | Full Range | $CO_2$, $CH_3CN/H_2O$, Water-Solid | 21 |
| $Bi_3TiNbO_9$ nanosheets | 20.91 (CO) | N.A. | AM1.5 G | $CO_2$, $H_2O$, Gas-Solid | 22 |
| BTA-PYTA | 77.8 (CO) | N.A. | λ>400 | $O_2$, $H_2O$, Water-Solid | 23 |

**References**


1 C. Yec, H. Zeng, *Chem. Mater.,* 2012, **24**, 1917.
2 H. Bader, V. Sturzenegger, J. Hoigné, *Water Res.,* 1988, **22**, 1109
3 E. Landaeta, N. I. Kadosh and Z. D. Schultz, *ACS Catal.,* 2023, **13**: 1638-1648.
4 X. Meng, H. Huang, X. Zhang, L. Hu, H. Tang, M. Han, F. Zheng and H. Wang, *Adv. Funct. Mater.,* 2024, 2312719.
5 A. Herzog, A. Bergmann, H. S. Jeon, J. Timoshenko, S. Kühl, C. Rettenmaier, M. Lopez Luna, F. T. Haase and B. Roldan Cuenya, *Angew. Chem. Int. Ed.,* 2021, **60**, 7426.
6 M. E. Aguirre, R. Zhou, A. J. Eugene, M. I. Guzman and M. A. Grela, *Appl. Catal. B*, 2017, **217**, 485-493.
7 Z. Xiong, Z. Lei, C.-C. Kuang, X. Chen, B. Gong, Y. Zhao, J. Zhang, C. Zheng and J. C. S. Wu, *Appl. Catal. B*, 2017, **202**, 695-703.
8 W. Wang, W. Zhang, C. Deng, H. Sheng and J. Zhao, *Angew. Chem. Int. Ed.*, **63**, e202317969
9 C. Du, J. Sheng, F. Zhong, Y. He, H. Liu, Y. Sun and F. Dong, *Proc. Natl. Acad. Sci. U.S.A.*, 2024, **121**, e2315956121.
10 B. Wang, H. Chen, W. Zhang, H. Liu, Z. Zheng, F. Huang, J. Liu, G. Liu, X. Yan, Y.-X. Weng, H. Li, Y. She, P. K. Chu and J. Xia, *Adv. Mater.*, 2024, 2312676.
11 J.-R. Huang, W.-X. Shi, S.-Y. Xu, H. Luo, J. Zhang, T.-B. Lu and Z.-M. Zhang, *Adv. Mater.*, 2023, 2306906.
12 S. Yin, X. Zhao, E. Jiang, Y. Yan, P. Zhou and P. Huo, *Energy Environ. Sci.*, 2022, **15**, 1556-1562.
13 Y. Duan, Y. Wang, W. Zhang, J. Zhang, C. Ban, D. Yu, K. Zhou, J. Tang, X. Zhang, X. Han, L. Gan, X. Tao and X. Zhou, *Adv. Funct. Mater.*, 2023, **33**, 2301729.
14 X. Li, L. Li, G. Chen, X. Chu, X. Liu, C. Naisa, D. Pohl, M. Löffler and X. Feng, *Nat. Commun.*, 2023, **14**, 4034
15 M. Lu, M. Zhang, J. Liu, T.-Y. Yu, J.-N. Chang, L.-J. Shang, S.-L. Li and Y.-Q. Lan, *J. Am. Chem. Soc.*, 2022, **144**, 1861-1871.
16 Z.-B. Fang, T.-T. Liu, J. Liu, S. Jin, X.-P. Wu, X.-Q. Gong, K. Wang, Q. Yin, T.-F. Liu, R. Cao and H.-C. Zhou, *J. Am. Chem. Soc.*, 2020, **142**, 12515-12523.
17 L. Liu, H. Huang, Z. Chen, H. Yu, K. Wang, J. Huang, H. Yu and Y. Zhang, *Angew. Chem. Int. Ed.*, 2021, **60**, 18303-18308.
18 J. Wang, E. Kim, D. P. Kumar, A. P. Rangappa, Y. Kim, Y. Zhang and T. K. Kim, *Angew. Chem. Int. Ed.*, 2022, **61**, e202113044.
19 Y. Cao, L. Guo, M. Dan, D. E. Doronkin, C. Han, Z. Rao, Y. Liu, J. Meng, Z. Huang, K. Zheng, P. Chen, F. Dong and Y. Zhou, *Nat. Commun.*, 2021, **12**, 1675.
20 M. Sayed, F. Xu, P. Kuang, J. Low, S. Wang, L. Zhang and J. Yu, Nat. Commun., 2021, **12**, 4936.
21 F. Xu, K. Meng, B. Cheng, S. Wang, J. Xu and J. Yu, *Nat. Commun.*, 2020, **11**, 4613.
22 H. Yu, F. Chen, X. Li, H. Huang, Q. Zhang, S. Su, K. Wang, E. Mao, B. Mei, G. Mul, T. Ma and Y. Zhang, *Nat. Commun.*, 2021, **12**, 4594.
23 S. Mohata, R. Das, K. Koner, M. Riyaz, K. Das, S. Chakraborty, Y. Ogaeri, Y. Nishiyama, S. C Peter and R. Banerjee, *J. Am. Chem. Soc.*, 2023, **145**, 23802-23813.